Observation of micropolar modes in the transmission of acoustic waves at oblique incidence by polystyrene plates.

Christian Meso, Hervé Franklin, Erick Ogam, Zine El Abiddine Fellah

Observation of micropolar modes in the transmission of acoustic waves at oblique incidence by polystyrene plates

C. Meso,[1, a] H. Franklin,[2] E. Ogam,[1] and Z.E.A. Fellah[1]

[1] *Aix Marseille Univ, CNRS, Centrale Med, LMA, Marseille, France*

[2] *Laboratoire Ondes et Milieux Complexes LOMC UMR CNRS 6294, 75 rue Bellot, Université Le Havre Normandie, Le Havre, France*

(Dated: 12 September 2024)

This study investigates micropolar plates through the analysis of transmitted acoustic waves at various incident angles. Using a combined theoretical and experimental approach, we explore the non-classical elasto-dynamic behavior of these materials. Theoretical transmission coefficients are tailored to highlight generalized Lamb modes and a new type of vibration modes called micropolar modes, considering the constant thickness of the plate and the effects of material micropolarity on linear elasticity. Overlaying diverse transmission coefficients for different angles provides insight into micropolar behavior, aiding in the understanding of mode evolution in the frequency domain and in the estimation of the critical angle. We employ two types of low-density closed-cell foams made from polystyrene (expanded in one case, extruded in the other), covering a frequency range of 4 to 60 kHz using a tweeter loudspeaker and a microphone integrated with a National Instruments acquisition system. Identification of the plates first vibration mode is facilitated by the frequency range rich in low frequencies. Additionally, all responses exhibit supersonic velocities with substantial attenuations. The originality of this paper is twofold : it provides theoretical predictions of micropolar modes, along with their experimental observations above a critical angle of incidence. Consequently, this research enriches our understanding of micropolar materials and their potential contribution to effective noise reduction strategies in acoustic engineering.

[a] meso@lma.cnrs-mrs.fr

I. INTRODUCTION

In 1909, the Cosserat brothers, Eugène and François, introduced a variation of continuum mechanics as documented in their work (see Cosserat and Cosserat (1909)), which gave rise to formulations of polar continua incorporating stress couples, as discussed in subsequent studies by Koiter (1969); Maugin and Metrikine (2010); Mindlin (1965); Mindlin *et al.* (1962); Toupin (1962); and others. The linear theory of polar media, including body microinertia effects, is known as the mechanics of micropolar continua in the studies by Eringen (1966, 1999, 2012); Hassanpour and Heppler (2017); Kafadar and Eringen (1971). We focus here on "micropolar linear elastic media", a combination of words that designates elastic materials whose elastic behavior is linear (reversibility of deformations in response to mechanical stresses) and influenced by phenomena or characteristics at the microscopic scale (each material point in the medium is granted a general intrinsic deformation -like a small deformable ellipsoid, hence six additional degrees of freedom- in addition to the usual translational degree of freedom. It is then, according to the classification of Eringen, a micromorphic medium, the rigidification of this microstructure reducing the medium to a micropolar or Cosserat medium).

By revealing the prediction of micropolar modes of vibration and observing them experimentally above a critical angle of incidence, our work is part of a dynamic evolution of research into the micropolar behavior of materials in response to acoustic waves. Our object is to investigate the properties of the acoustic transmission by a micropolar linear elastic plate immersed in a fluid and, by extension, of the modes of vibration. Here, the

transmission (and at the same time the reflection) coefficients are constructed with the aim of generalizing the formulas previously introduced for plates in classical elasticity, for example by Viktorov (1967) and later by Fiorito *et al.* (1979) (Fiorito, Madigosky and Überall (FMU)). An exhaustive list of studies on the subject would be extensive, and may contain omissions. For classical elasticity, FMU's work introduced a clear formalism for interpreting reflection and transmission coefficients. A similar approach, adapted for the S-matrix method provided by Franklin *et al.* (2001), could aid in analyzing Lamb and micropolar modes, albeit without resonance considerations.

The paper is structured as follows : Sec. II provides a brief overview of micropolar elastic materials. In Sec. III, equations describing a micropolar elastic plate separating two fluids are presented. Sec. IV outlines the exact forms of reflection and transmission coefficients for such a plate, allowing the presupposition of symmetric and antisymmetric modes. Sec. V presents numerical results, including illustrations of transmission coefficients for two micropolar plates - one expanded polystyrene (EPS) plate and one extruded polystyrene (XPS) plate - based on data from Ogam *et al.* (2021). Experimental results and comparisons with calculations are detailed in Sec. VI, followed by a conclusion.

II. BACKGROUND ON WAVES IN MICROPOLAR ELASTIC MEDIA

Parfitt and Eringen (1969) showed that four basic plane harmonic waves (the time dependence $e^{-i\omega t}$ is considered, ω being the angular frequency) travel in micropolar linear elastic medium at four distinct phase velocities : (i) a longitudinal displacement wave at speed v_1, (ii) a longitudinal micro-rotation wave at speed v_2 with microrotation in the direction

of propagation, (iii) two transverse (displacement and microrotation) waves of respective velocities v_3 and v_4. The expressions of these phase velocities extracted from Eringen (2012) are

$$v_1^2 = c_1^2, \quad v_2^2 = \frac{c_3^2}{1 - \omega_0^2/\omega^2}, \tag{1}$$

$$v_3^2 = \frac{\omega^2}{r - \sqrt{r^2 - s}}, \quad v_4^2 = \frac{\omega^2}{r + \sqrt{r^2 - s}}, \tag{2}$$

provided $r^2 - s \geq 0$ (this condition, as well as positive values for v_3^2 and v_4^2, prevails when $\omega^2 > \omega_0^2$), where

$$r = \frac{1}{2}\left(1 + \frac{c_2^2}{c_4^2}\right)\frac{\omega^2}{c_2^2} - \left(1 - \frac{J\omega_0^2}{4c_2^2}\right)\frac{\omega_0^2}{2c_4^2}, \quad s = \frac{\omega^2\left(\omega^2 - \omega_0^2\right)}{c_2^2 c_4^2}. \tag{3}$$

Above, $c_1^2 = \frac{\lambda+2\mu+K}{\rho}$, $c_2^2 = \frac{\mu+K}{\rho}$, $c_3^2 = \frac{\alpha+\beta+\gamma}{\rho J}$, $c_4^2 = \frac{\gamma}{\rho J}$ and $\omega_0^2 = \frac{2K}{\rho J}$ where ρ is the mass density of the medium. In the phase velocities c_1 and c_2, the quantities λ and μ represent Lamé moduli, K is Cosserat's couple modulus (in relation with the micropolar state). In the phase velocities c_3 and c_4, α, β and γ are rotational micro-inertia constants which, when divided by the microinertia constant J, yield moduli (γ is often referred to as the twist coefficient). Parfitt and Eringen (1969) also studied the problem of reflection of plane waves from the flat boundary of a micropolar elastic half-space. Later, Kumar *et al.* (2001) studied the reflection and transmission of elastic waves at viscous liquid-micropolar elastic solid interfaces, while Singh and Tomar (2008) examined the reflection and transmission of elastic waves at viscous liquid-micropolar elastic solid interfaces. Recently, Ogam *et al.* (2021) published a paper on experimental study of reflection and transmission by several micropolar elastic plates - air-filled closed-cell polystyrene panels assumed to obey Cosserat

elasticity - in air. The micropolar elastic materials (XPS and EPS) considered herein are the same they used.

III. EQUATIONS FOR A MICROPOLAR PLATE SEPARATING TWO FLUIDS

A plate of constant thickness $2h$ obeying linear isotropic micropolar elastic constitutive equations is in contact on the face Γ_a with a perfect fluid (a) of mass density ρ_a and sound phase velocity c_a, and on the face Γ_b with another perfect fluid (b) of mass density ρ_b and sound phase velocity c_b. The plane problem of reflection and transmission to be addressed is sketched in Fig. 1.

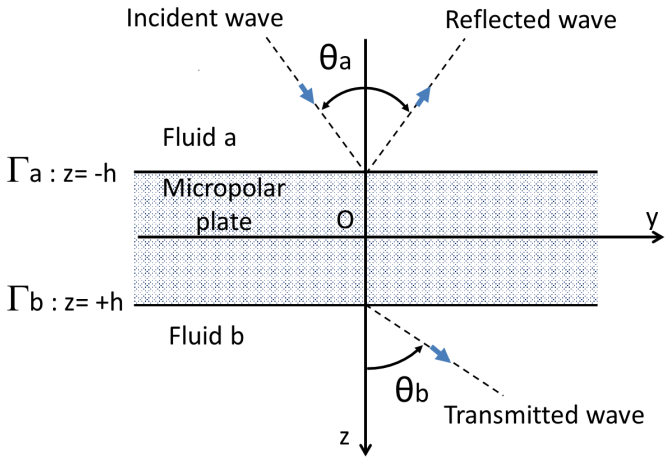

FIG. 1. A micropolar plate impinged by an incident wave from fluid a.

A. Displacements and pressures in the fluids

Let $\psi_a(y,z,t) \equiv \psi_a$ and $\psi_b(y,z,t) \equiv \psi_b$ be scalar displacement potentials in the fluids. In fluid (a), the displacement along the z-axis normal to the faces and pressure are given by

$u_{az} = \psi_{a,z}$ and $P_a = -\rho_a \psi_{a,tt}$. In fluid (b), we have $u_{bz} = \psi_{b,z}$ and $P_b = -\rho_b \psi_{b,tt}$. Indices following a comma indicate partial differentiation (with respect to the space variable z or time t). In this context, assuming the existence of incident (I) and reflected (R) waves on one side and transmitted (T) waves on the other side, we can write the potentials :

$$\psi_a = \psi_{aI} + \psi_{aR}, \quad \psi_b = \psi_{bT}, \tag{4}$$

where

$$\psi_{aI} = A_{aI} e^{ik_{az}z} e(y,t), \quad \psi_{aR} = A_{aR} e^{-ik_{az}z} e(y,t), \tag{5}$$

and

$$\psi_{bT} = A_{bT} e^{ik_{bz}z} e(y,t). \tag{6}$$

In the foregoing, $e(y,t) = e^{i(k_y y - \omega t)}$, $k_y = k_a \sin\theta_a = k_b \sin\theta_b$, $k_{az} = k_a \cos\theta_a$ and $k_{bz} = k_b \cos\theta_b$ where $k_a = \frac{\omega}{c_a}$, $k_b = \frac{\omega}{c_b}$ (θ_a, θ_b are the angles of incidence and of transmission shown in Fig. 1).

B. Displacements, stress and couple stress tensors in the plate

In the plate, let $q(y,z,t) \equiv q$ be a scalar potential and let $\Pi_x(y,z,t) \equiv \Pi_x$, $\Theta_y(y,z,t) \equiv \Theta_y$, $\Theta_z(y,z,t) \equiv \Theta_z$ be components of vector potentials. The particle displacement along the z-axis is given by

$$u_z = q_{,z} - \Pi_{x,y}. \tag{7}$$

The stress tensor components σ and the couple stress tensor components $\mathbf{m}$ provided in the following equations can be obtained by referring to Equations (5.17.2) of Eringen (2012). In these equations, the potentials $\bar{U}$ and $\bar{\phi}$ are substituted for Π_x and $\Theta_{z,y} - \Theta_{y,z}$ respectively.

However, it is important to note that using $\bar{\phi}$ instead of $\Theta_{z,y} - \Theta_{y,z}$ may result in a slightly different interpretation of the vibration modes of a plate in vacuum. Further elaboration is provided subsequently.

$$\sigma_{zz} = \lambda\nabla^2 q + (2\mu + K)(q_{,zz} - \Pi_{x,zy}), \tag{8}$$

$$\sigma_{zy} = (2\mu + K)q_{,yz} + (\mu + K)\Pi_{x,zz} - \mu\Pi_{x,yy} + K(\Theta_{z,y} - \Theta_{y,z}), \tag{9}$$

$$m_{zx} = \gamma(\Theta_{z,zy} - \Theta_{y,zz}). \tag{10}$$

The following expansions can be considered for the quantities introduced above :

$$q = [a_1 \cos(k_{1z}z) + b_1 \sin(k_{1z}z)]\, e(y,t) = \left[q^+(z) + q^-(z)\right] e(y,t), \tag{11}$$

$$\Pi_x = [\Pi_{3x}(z) + \Pi_{4x}(z)]\, e(y,t), \tag{12}$$

$$\Theta_y = [\eta_{3y}\Pi_{3x}(z) + \eta_{4y}\Pi_{4x}(z)]\, e(y,t), \tag{13}$$

and

$$\Theta_z = [\eta_{3z}\Pi_{3x}(z) + \eta_{4z}\Pi_{4x}(z)]\, e(y,t), \tag{14}$$

where

$$\Pi_{3x}(z) = A_3 \cos(k_{3z}z) + B_3 \sin(k_{3z}z) = \Pi^+_{3x}(z) + \Pi^-_{3x}(z), \tag{15}$$

and

$$\Pi_{4x}(z) = A_4 \cos(k_{4z}z) + B_4 \sin(k_{4z}z) = \Pi^+_{4x}(z) + \Pi^-_{4x}(z). \tag{16}$$

In the foregoing equations, $k_{pz} = +(k_p^2 - k_y^2)^{\frac{1}{2}}$ where $k_p = \frac{\omega}{v_p}$ $(p = 1, 3, 4)$ and

$$\eta_{py} = \frac{-i\omega_0^2}{2k_p^2\left(v_p^2 - \frac{\omega_0^2}{k_p^2} - c_4^2\right)} k_{pz}, \quad (p = 3, 4) \tag{17}$$

and

$$\eta_{pz} = \frac{i\omega_0^2}{2k_p^2\left(v_p^2 - \frac{\omega_0^2}{k_p^2} - c_4^2\right)} k_y, \quad (p = 3, 4). \tag{18}$$

Note that expressions like Π_{px} $(p = 3, 4)$ result from a superposition of incident and reflected waves propagating in the plate. Our purpose, A_{aI} being fixed, is now other side the amplitudes A_{aR} and A_{bT}.

C. Boundary conditions

The four boundary conditions to consider at the discontinuities Γ_p $(p = a, b)$ are

$$u_z = u_{pz}, \quad \sigma_{zz} = -P_p, \quad \sigma_{zy} = 0, \quad m_{zx} = 0. \tag{19}$$

Based on the above definitions, it can be shown that

$$\begin{aligned}
&\sigma_{zz} + i\tfrac{\rho_a\omega^2}{k_{az}} u_z = -2i\rho_a\omega^2\psi_{aI}, \\
&\sigma_{zz} - i\tfrac{\rho_a\omega^2}{k_{az}} u_z = -2i\rho_a\omega^2\psi_{aR}, \\
&\sigma_{zy} = 0, \\
&m_{zx} = 0,
\end{aligned} \tag{20}$$

at the discontinuity Γ_a and

$$\begin{aligned}
&\sigma_{zz} + i\tfrac{\rho_b\omega^2}{k_{bz}} u_z = -2i\rho_b\omega^2\psi_{bR}, \\
&\sigma_{zz} - i\tfrac{\rho_b\omega^2}{k_{bz}} u_z = 0, \\
&\sigma_{zy} = 0, \\
&m_{zx} = 0,
\end{aligned} \tag{21}$$

at the discontinuity Γ_b. In order to exploit the set of Eqs. (20)-(21), it is necessary to find

displacement, stress and torque stress as functions of the potentials introduced above. At every point inside the plate, we obtain from Eqs. (8)-(10) and Eqs. (12)-(14)

$$\sigma_{zz} = (\mu + K)\left\{\sigma_2 q - i\Sigma\Pi_{3x,z} - i\Sigma\Pi_{4x,z}\right\}, \tag{22}$$

$$\sigma_{zy} = (\mu + K)\left\{i\Sigma q_{,z} + \Sigma_3\Pi_{3x} + \Sigma_4\Pi_{4x} - \mathcal{K}\eta_{3y}\Pi_{3x,z} - \mathcal{K}\eta_{4y}\Pi_{4x,z}\right\}, \tag{23}$$

and

$$m_{zx} = \gamma\left(ik_y\eta_{3z}\Pi_{3x,z} + ik_y\eta_{4z}\Pi_{4x,z} + k_{3z}^2\eta_{3y}\Pi_{3x} + k_{4z}^2\eta_{4y}\Pi_{4x}\right), \tag{24}$$

where

$$\sigma_2 = (2 - \mathcal{K})k_y^2 - l_2^2, \tag{25}$$

$$\Sigma = (2 - \mathcal{K})k_y, \tag{26}$$

and

$$\Sigma_p = (2 - \mathcal{K})k_y^2 - k_p^2 + ik_y\mathcal{K}\eta_{pz}, \quad (p = 3, 4). \tag{27}$$

Above, $\mathcal{K} = \frac{K}{\mu+K}$, $l_2^2 = \frac{\omega^2}{c_2^2}$, $k_3^2 = \frac{\omega^2}{v_3^2}$ and $k_4^2 = \frac{\omega^2}{v_4^2}$. By using the boundary condition $\sigma_{zy} = 0$, an expression for $q_{,z}$ is derived

$$q_{,z} = i\left(\tilde{\Sigma}_3\Pi_{3x} + \tilde{\Sigma}_4\Pi_{4x} - \tilde{\epsilon}_3\Pi_{3x,z} - \tilde{\epsilon}_4\Pi_{4x,z}\right), \tag{28}$$

where

$$\tilde{\Sigma}_p = \frac{\Sigma_p}{\Sigma}, \quad \tilde{\epsilon}_p = \frac{\mathcal{K}\eta_{py}}{\Sigma}. \quad (p = 3, 4). \tag{29}$$

It can be exploited to write the displacements, Eq. (7), at the discontinuities as

$$u_z = i\left(\mathfrak{u}_3\Pi_{3x} + \mathfrak{u}_4\Pi_{4x} - \tilde{\epsilon}_3\Pi_{3x,z} - \tilde{\epsilon}_4\Pi_{4x,z}\right), \tag{30}$$

where

$$\mathfrak{u}_p = \tilde{\Sigma}_p - k_y, \quad (p = 3, 4). \tag{31}$$

1. *Consequences of applying $\sigma_{zy} = 0$ and $m_{zx} = 0$ at both Γ_a and Γ_b*

The fact that $\sigma_{zy} = 0$ at $z = -h$ and $z = h$ yields the following two equations

$$-q^+_{,z}(h) + q^-_{,z}(h) = i\sum_{p=3}^{4} \tilde{\Sigma}_p \left[\Pi^+_{px}(h) - \Pi^-_{px}(h)\right] - i\sum_{p=3}^{4} \tilde{\epsilon}_p \left[-\Pi^+_{px,z}(h) + \Pi^-_{px,z}(h)\right], \tag{32}$$

and

$$q^+_{,z}(h) + q^-_{,z}(h) = i\sum_{p=3}^{4} \tilde{\Sigma}_p \left[\Pi^+_{px}(h) + \Pi^-_{px}(h)\right] - i\sum_{p=3}^{4} \tilde{\epsilon}_p \left[\Pi^+_{px,z}(h) + \Pi^-_{px,z}(h)\right]. \tag{33}$$

By adding these two equations on the one hand, by subtracting them on the other hand, one ends up with

$$q^-_{,z}(h) = i\sum_{p=3}^{4} \tilde{\Sigma}_p \Pi^+_{px}(h) - i\sum_{p=3}^{4} \tilde{\epsilon}_p \Pi^-_{px,z}(h), \tag{34}$$

and

$$q^+_{,z}(h) = i\sum_{p=3}^{4} \tilde{\Sigma}_p \Pi^-_{px}(h) - i\sum_{p=3}^{4} \tilde{\epsilon}_p \Pi^+_{px,z}(h). \tag{35}$$

Let us make use now of relationships linking the derivatives $q^\mp_{,z}$ to $q^\mp$, that is,

$$q^+_{,z}(h) = -k_{1z} \tan(k_{1z}h) q^+(h), \tag{36}$$

and

$$q^-_{,z}(h) = k_{1z} \cot(k_{1z}h) q^-(h). \tag{37}$$

Note that the same relationships hold if q is replaced by Π_{px}. We derive from Eqs. (33) and (34)

$$q^-(h) = \frac{i}{k_{1z}\cot(k_{1z}h)} \left[\sum_{p=3}^{4} \tilde{\Sigma}_p \Pi^+_{px}(h) - \sum_{p=3}^{4} \tilde{\epsilon}_p k_{pz} \cot(k_{pz}h) \Pi^-_{px}(h)\right], \tag{38}$$

and

$$q^+(h) = \frac{-i}{k_{1z}\tan(k_{1z}h)} \left[\sum_{p=3}^{4} \tilde{\Sigma}_p \Pi^-_{px}(h) + \sum_{p=3}^{4} \tilde{\epsilon}_p k_{pz} \tan(k_{pz}h) \Pi^+_{px}(h)\right]. \tag{39}$$

For its part, the equation $m_{zx} = 0$ considered at the discontinuities $z = -h$ and $z = h$ leads, on account of Eq. (24), to

$$\sum_{p=3}^{4} \mathcal{S}_p \Pi_{px}^{-}(h) + \sum_{p=3}^{4} k_{pz}^2 \eta_{py} \Pi_{px}^{+}(h) = 0, \tag{40}$$

and

$$-\sum_{p=3}^{4} \mathcal{A}_p \Pi_{px}^{+}(h) + \sum_{p=3}^{4} k_{pz}^2 \eta_{py} \Pi_{px}^{-}(h) = 0. \tag{41}$$

where $\mathcal{S}_p = ik_y \eta_{pz} k_{pz} \cot(k_{pz} h)$ and $\mathcal{A}_p = ik_y \eta_{pz} k_{pz} \tan(k_{pz} h)$.

2. *Boundary conditions at* $\boldsymbol{\Gamma_a}$

Consider the first two boundary conditions in Eq. (20). Using the results detailed in the preceding section leads to

$$\sum_{p=3}^{4} \left(C_{aSp}^{-} + i\tau_{ap} \right) \Pi_{px}^{-} + \sum_{p=3}^{4} \left(C_{aAp}^{-} - i\tau_{ap} \right) \Pi_{px}^{+} = -2i \frac{\rho_a k_{1z}}{\rho} \Sigma l_2^2 \psi_{aI}, \tag{42}$$

$$\sum_{p=3}^{4} \left(C_{aSp}^{+} - i\tau_{ap} \right) \Pi_{px}^{-} + \sum_{p=3}^{4} \left(C_{aAp}^{+} + i\tau_{ap} \right) \Pi_{px}^{+} = -2i \frac{\rho_a k_{1z}}{\rho} \Sigma l_2^2 \psi_{aR}, \tag{43}$$

where

$$C_{aSp}^{-} = \sigma_2 \Sigma_p \cot(k_{1z} h) - \mathfrak{C}_{aAp}^{+-} k_{pz} \cot(k_{pz} h), \tag{44}$$

$$C_{aAp}^{-} = \sigma_2 \Sigma_p \tan(k_{1z} h) + \mathfrak{C}_{aSp}^{--} k_{pz} \tan(k_{pz} h), \tag{45}$$

$$C_{aSp}^{+} = \sigma_2 \Sigma_p \cot(k_{1z} h) - \mathfrak{C}_{aAp}^{++} k_{pz} \cot(k_{pz} h), \tag{46}$$

$$C_{aAp}^{+} = \sigma_2 \Sigma_p \tan(k_{1z} h) + \mathfrak{C}_{aSp}^{-+} k_{pz} \tan(k_{pz} h). \tag{47}$$

and

$$\tau_{ap} = \frac{\rho_a k_{1z}}{\rho k_{az}} \Sigma l_2^2 \mathfrak{u}_p. \tag{48}$$

In the foregoing expressions, for the sake of compactness of the mathematical expressions, we introduced

$$\mathfrak{C}_{aAp}^{+-} = \sigma_2 \epsilon_p \tan(k_{1z} h) + i W_{ap}^{-}, \tag{49}$$

$$\mathfrak{C}_{aSp}^{--} = \sigma_2 \epsilon_p \cot(k_{1z} h) - i W_{ap}^{-}, \tag{50}$$

$$\mathfrak{C}_{aAp}^{++} = \sigma_2 \epsilon_p \tan(k_{1z} h) + i W_{ap}^{+}, \tag{51}$$

$$\mathfrak{C}_{aSp}^{-+} = \sigma_2 \epsilon_p \cot(k_{1z} h) - i W_{ap}^{+}, \tag{52}$$

where, since $\epsilon_p = \Sigma \tilde{\epsilon}_p$

$$W_{ap}^{\mp} = i\Sigma^2 k_{1z} \mp \frac{\rho_a k_{1z}}{\rho k_{az}} l_2^2 \epsilon_p. \tag{53}$$

We can notice that C_{aAp}^{+} and C_{aAp}^{-} involve tangent functions but also the cotangent function through the terms $\mathfrak{C}_{aSp}^{++}$ and $\mathfrak{C}_{aSp}^{--}$. For their part, C_{aSp}^{+} and C_{aSp}^{-} involve cotangent functions but also the tangent function through the terms $\mathfrak{C}_{aAp}^{++}$ and $\mathfrak{C}_{aAp}^{--}$.

3. Boundary conditions at Γ_b

Consider now the first two boundary conditions in Eq. (21). Work similar to that in the previous section changes them to

$$-\sum_{p=3}^{4} \left(C_{bSp}^{-} - i\tau_{bp} \right) \Pi_{px}^{-} + \sum_{p=3}^{4} \left(C_{bAp}^{-} + i\tau_{bp} \right) \Pi_{px}^{+} = 2i \frac{\rho_b k_{1z}}{\rho} \Sigma l_2^2 \psi_{bT}, \tag{54}$$

$$-\sum_{p=3}^{4} \left(C_{bSp}^{+} + i\tau_{bp} \right) \Pi_{px}^{-} + \sum_{p=3}^{4} \left(C_{bAp}^{+} - i\tau_{bp} \right) \Pi_{px}^{+} = 0, \tag{55}$$

where

$$C_{bSp}^{-} = \sigma_2 \Sigma_p \cot(k_{1z} h) + \mathfrak{C}_{bAp}^{--} k_{pz} \cot(k_{pz} h), \tag{56}$$

$$C^{-}_{bAp} = \sigma_2 \Sigma_p \tan(k_{1z} h) - \mathfrak{C}^{+-}_{bSp} k_{pz} \tan(k_{pz} h), \tag{57}$$

$$C^{+}_{bSp} = \sigma_2 \Sigma_p \cot(k_{1z} h) + \mathfrak{C}^{-+}_{bAp} k_{pz} \cot(k_{pz} h), \tag{58}$$

$$C^{+}_{bAp} = \sigma_2 \Sigma_p \tan(k_{1z} h) - \mathfrak{C}^{++}_{bSp} k_{pz} \tan(k_{pz} h), \tag{59}$$

and

$$\tau_{bp} = \frac{\rho_b k_{1z}}{\rho k_{bz}} \Sigma l_2^2 \mathfrak{u}_p. \tag{60}$$

Above,

$$\mathfrak{C}^{--}_{bAp} = \sigma_2 \epsilon_p \tan(k_{1z} h) - i W^{-}_{bp}, \tag{61}$$

$$\mathfrak{C}^{+-}_{bSp} = \sigma_2 \epsilon_p \cot(k_{1z} h) + i W^{-}_{bp}, \tag{62}$$

$$\mathfrak{C}^{-+}_{bAp} = \sigma_2 \epsilon_p \tan(k_{1z} h) - i W^{+}_{bp}, \tag{63}$$

$$\mathfrak{C}^{++}_{bSp} = \sigma_2 \epsilon_p \cot(k_{1z} h) + i W^{+}_{bp}, \tag{64}$$

where

$$W^{\mp}_{bp} = i\Sigma^2 k_{1z} \mp \frac{\rho_b k_{1z}}{\rho k_{bz}} l_2^2 \epsilon_p. \tag{65}$$

IV. REFLECTION AND TRANSMISSION COEFFICIENTS AT OBLIQUE INCIDENCE

A. General expressions

To compute the reflection and transmission coefficients when a plane wave hits the plate from side Γ_a, we utilize Eqs. (42), (43), (54), (55), along with Eqs. (40) and (41). The resulting linear system comprises 6 equations with 6 unknowns, which can be expressed in matrix form :

$$\mathbf{M}.\mathbf{x} = \mathbf{s}, \tag{66}$$

where

$$\mathbf{M}=\begin{pmatrix} C^{-}_{aS3}+i\tau_{a3} & C^{-}_{aS4}+i\tau_{a4} & C^{-}_{aA3}-i\tau_{a3} & C^{-}_{aA4}-i\tau_{a4} & 0 & 0 \\ C^{+}_{aS3}-i\tau_{a3} & C^{+}_{aS4}-i\tau_{a4} & C^{+}_{aA3}+i\tau_{a3} & C^{+}_{aA4}+i\tau_{a4} & 2i\frac{\rho_a k_{1z}}{\rho}\Sigma l_2^2 & 0 \\ -(C^{-}_{bS3}-i\tau_{b3}) & -(C^{-}_{bS4}-i\tau_{b4}) & C^{-}_{bA3}+i\tau_{b3} & C^{-}_{bA4}+i\tau_{b4} & 0 & -2i\frac{\rho_b k_{1z}}{\rho}\Sigma l_2^2 \\ -(C^{+}_{bS3}+i\tau_{b3}) & -(C^{+}_{bS4}+i\tau_{b4}) & C^{+}_{bA3}-i\tau_{b3} & C^{+}_{bA4}-i\tau_{b4} & 0 & 0 \\ \mathcal{S}_3 & \mathcal{S}_4 & k_{3z}^2\eta_{3y} & k_{4z}^2\eta_{4y} & 0 & 0 \\ -k_{3z}^2\eta_{3y} & -k_{4z}^2\eta_{4y} & \mathcal{A}_3 & \mathcal{A}_4 & 0 & 0 \end{pmatrix}, \tag{67}$$

$$\mathbf{x} = \begin{pmatrix} \Pi_{3x}^{-} & \Pi_{4x}^{-} & \Pi_{3x}^{+} & \Pi_{4x}^{+} & \psi_{aR} & \psi_{aT} \end{pmatrix}^{T}, \tag{68}$$

and

$$\mathbf{s} = \begin{pmatrix} -2i\dfrac{\rho_a k_{1z}}{\rho}\Sigma l_2^2 \psi_{aI} & 0 & 0 & 0 & 0 & 0 \end{pmatrix}^{T}. \tag{69}$$

The use of Cramer's rule allows us to write the reflection and transmission coefficients as follows ($\psi_{aI} = A_{aI}e^{-ik_{az}h}$, $\psi_{aR} = A_{aR}e^{ik_{az}h}$, $\psi_{bT} = A_{bT}e^{-ik_{bz}h}$)

$$R_a = \frac{\psi_{aR}}{\psi_{aI}} = \frac{N_R}{\Delta}, \quad T_a = \frac{\psi_{bT}}{\psi_{aI}} = \frac{N_T}{\Delta}, \tag{70}$$

where Δ, N_R and N_T are the following 4×4 determinants

$$\Delta = \begin{vmatrix} C_{aS3}^{-} + i\tau_{a3} & C_{aS4}^{-} + i\tau_{a4} & C_{aA3}^{-} - i\tau_{a3} & C_{aA4}^{-} - i\tau_{a4} \\ -(C_{bS3}^{+} + i\tau_{b3}) & -(C_{bS4}^{+} + i\tau_{b4}) & C_{bA3}^{+} - i\tau_{b3} & C_{bA4}^{+} - i\tau_{b4} \\ \mathcal{S}_3 & \mathcal{S}_4 & k_{3z}^2\eta_{3y} & k_{4z}^2\eta_{4y} \\ -k_{3z}^2\eta_{3y} & -k_{4z}^2\eta_{4y} & \mathcal{A}_3 & \mathcal{A}_4 \end{vmatrix}, \tag{71}$$

$$N_R = \begin{vmatrix} C_{aS3}^{+} - i\tau_{a3} & C_{aS4}^{+} - i\tau_{a4} & C_{aA3}^{+} + i\tau_{a3} & C_{aA4}^{+} + i\tau_{a4} \\ -(C_{bS3}^{+} + i\tau_{b3}) & -(C_{bS4}^{+} + i\tau_{b4}) & C_{bA3}^{+} - i\tau_{b3} & C_{bA4}^{+} - i\tau_{b4} \\ \mathcal{S}_3 & \mathcal{S}_4 & k_{3z}^2\eta_{3y} & k_{4z}^2\eta_{4y} \\ -k_{3z}^2\eta_{3y} & -k_{4z}^2\eta_{4y} & \mathcal{A}_3 & \mathcal{A}_4 \end{vmatrix}, \tag{72}$$

and

$$N_T = \frac{\rho_a}{\rho_b} \begin{vmatrix} -(C^-_{bS3} - i\tau_{b3}) & -(C^-_{bS4} - i\tau_{b4}) & C^-_{bA3} + i\tau_{b3} & C^-_{bA4} + i\tau_{b4} \\ -(C^+_{bS3} + i\tau_{b3}) & -(C^+_{bS4} + i\tau_{b4}) & C^+_{bA3} - i\tau_{b3} & C^+_{bA4} - i\tau_{b4} \\ \mathcal{S}_3 & \mathcal{S}_4 & k^2_{3z}\eta_{3y} & k^2_{4z}\eta_{4y} \\ -k^2_{3z}\eta_{3y} & -k^2_{4z}\eta_{4y} & \mathcal{A}_3 & \mathcal{A}_4 \end{vmatrix}. \tag{73}$$

B. Comparison with the classical elastic plate

Working on a classical elastic plate instead of a micropolar plate, it is appropriate to set $K = 0$ and $\gamma = 0$ in Eqs. (8) and (9). It follows that

$$\sigma_{zz} = \lambda \nabla^2 q + 2\mu(q_{,zz} - \Pi_{x,zy}), \tag{74}$$

$$\sigma_{zy} = 2\mu q_{,yz} + \mu \left(\Pi_{x,zz} - \Pi_{x,yy}\right). \tag{75}$$

The scalar potential q remains unchanged while the vector potential Π_x takes a simpler form $\Pi_x = \left[\Pi^+_{2x}(z) + \Pi^-_{2x}(z)\right] e(y,t)$, where $\Pi^+_{2x}(z) = A_2 \cos(k_{2z} z)$ and $\Pi^-_{2x}(z) = B_2 \sin(k_{2z} z)$. Here, $k_{2z} = +(k_2^2 - k_y^2)^{\frac{1}{2}}$ where $k_2 = \frac{\omega}{c_2}$ is the wavenumber for the shear wave ($c_2^2 = \frac{\mu}{\rho}$). Using the set of boundary conditions, Eqs. (20) and (21), after having excluded $m_{zx} = 0$ (absence of micropolar effects), we get the linear system

$$\mathbf{M}'.\mathbf{x}' = \mathbf{s}', \tag{76}$$

where

$$\mathbf{M}' = \begin{pmatrix} C_S - i\tau_a & C_A + i\tau_a & 0 & 0 \\ C_S + i\tau_a & C_A - i\tau_a & -2ik_y k_{1z}\frac{2\rho_a}{\rho}k_2^2 & 0 \\ -(C_S + i\tau_b) & C_A - i\tau_b & 0 & 2ik_y k_{1z}\frac{2\rho_b}{\rho}k_2^2 \\ -(C_S - i\tau_b) & C_A + i\tau_b & 0 & 0 \end{pmatrix}, \tag{77}$$

$$\mathbf{x}' = \begin{pmatrix} \Pi_x^- & \Pi_x^+ & \psi_{aR} & \psi_{aT} \end{pmatrix}^T, \tag{78}$$

and

$$\mathbf{s}' = \begin{pmatrix} 2i\frac{\rho_a k_{1z}}{\rho}\Sigma l_2^2 \psi_{aI} & 0 & 0 & 0 \end{pmatrix}^T. \tag{79}$$

Above,

$$C_{aS} = \sigma_2^2 \cot(k_{1z}h) + 4k_y^2 k_{1z}k_{2z}\cot(k_{2z}h), \tag{80}$$

$$C_{aA} = \sigma_2^2 \tan(k_{1z}h) + 4k_y^2 k_{1z}k_{2z}\tan(k_{2z}h), \tag{81}$$

where, since $\mathcal{K} = 0$, σ_2, Eq. (25), reduces to $\sigma_2 = 2k_y^2 - l_2^2$. Note also that $\tau_a = k_2^4\frac{\rho_a k_{1z}}{\rho k_{az}}$ and $\tau_b = k_2^4\frac{\rho_b k_{1z}}{\rho k_{bz}}$. When the two faces of the plate are in contact with the same fluid (indices $b \equiv a$ everywhere), the reflection and transmission coefficients calculated from Eq. (76) are as follows

$$R_a = \frac{\psi_{aR}}{\psi_{aI}} = \frac{1}{2}\left[\frac{C_{aS} + i\tau_a}{C_{aS} - i\tau_a} + \frac{C_{aA} - i\tau_a}{C_{aA} + i\tau_a}\right], \tag{82}$$

$$T_a = \frac{\psi_{aT}}{\psi_{aI}} = \frac{1}{2}\left[\frac{C_{aS} + i\tau_a}{C_{aS} - i\tau_a} - \frac{C_{aA} - i\tau_a}{C_{aA} + i\tau_a}\right]. \tag{83}$$

The comparison of Eqs. (82)-(83) with their counterparts, Eqs. (70) to (73), shows the first problem of interpretation to solve when considering micropolar materials. The reflection and transmission coefficients for the micropolar plate derived from Eqs. (70) to (73) cannot

be split into the pure symmetrical $\frac{C_{aS}+i\tau_a}{C_{aS}-i\tau_a}$ and pure antisymmetrical $\frac{C_{aA}-i\tau_a}{C_{aA}+i\tau_a}$ ratios, as for the classical elastic plate.

V. NUMERICAL STUDY FOR XPS AND EPS PLATES IN AIR

XPS (Extruded polystyrene) and EPS (Expanded polystyrene) are air-filled ($\simeq 96\%$) closed-cell rigid foam (See Ogam *et al.* (2021); Ashby and Gibson (1997)). The physical properties are listed in Table I (E is Young's modulus, ν Poisson's ratio and ρ mass density). From the data, it is deduced that $\omega_0 \simeq 1.9306 \times 10^4$rd/s ($f_0 \simeq 0.307 \times 10^4$Hz) for XPS and $\omega_0 \simeq 1.1646 \times 10^4$rd/s ($f_0 \simeq 0.185 \times 10^4$Hz) for EPS. In the computations as well as in the experiments, the thickness of the XPS plate is $2h = 3.5$cm while that of EPS12 is $2h = 2.865$cm. The faces are in contact with air (mass density 1.29 kg/m^3 and sound phase velocity 330 m/s), so that $\theta_a = \theta_b = \theta$ everywhere.

TABLE I. Physical properties of the two micropolar elastic materials (from Ogam *et al.* (2021)).

Material	ρ (kg/m^3)	E (Mpa)	ν	K (MPa)	γ (MN)	J (N/m)
XPS	32	2.7	0.49	0.0510	0.57	2.35×10^{-5}
EPS	12	1.2	0.45	0.037	0.87	3.9×10^{-5}

We report in the plane (f, θ) the values of the modulus of the transmission coefficient, *i.e.* $|T_a|$ (Fig. 2 for XPS, and Fig. 3 for EPS). This makes it possible to sketch the modes of vibration of each plate (highlighted by the colors different from the dark blue color which,

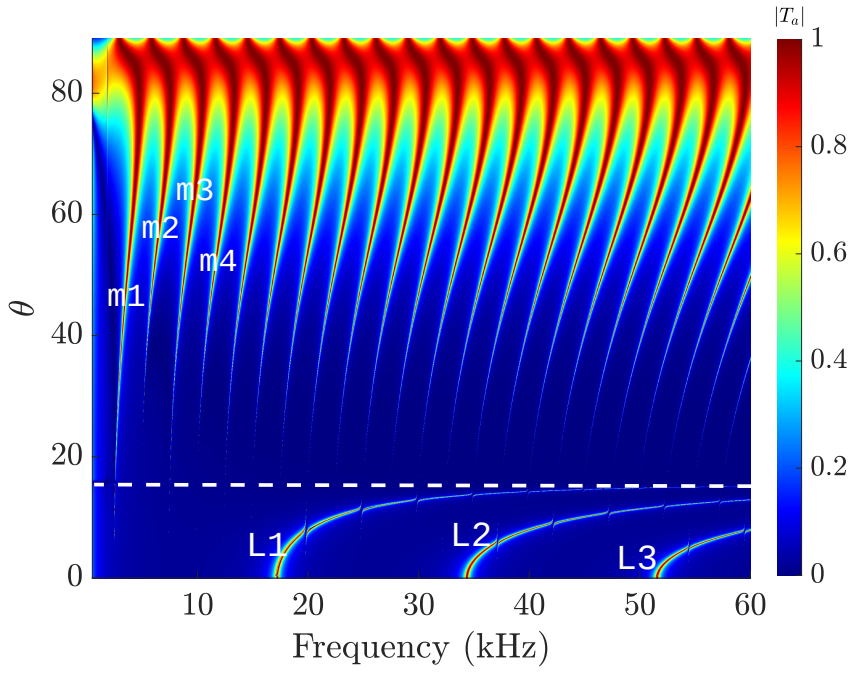

FIG. 2. (Colour on-line) Modulus of the transmission coefficient of a 3.5-cm-thick nonabsorbing XPS plate in air, in the frequency-angle of incidence plane (see data in Table I). This representation designs the generalized Lamb frequency spectrum L_j and the micropolar modes m_j $(j = 1, 2, ...)$.

corresponds to $T_a = 0$). The closer the color is to red, the closer the amplitude of the transmission coefficient is to 1. There is a correspondence between the modes drawn here and those that would be obtained by solving the dispersion equation $\Delta(k_y, f) = 0$. In the latter case, we would have called them eigenmodes of the plate. The position of the critical angle (dotted white line) is $\theta_C = 15.93°$ for XPS and $\theta_C = 32.25°$ for EPS12. As illustrated in the two figures, the critical angle defines an upper angular limit beyond which we no longer encounter the modes L_j $(j = 1, ...)$. In the region $\theta < \theta_C$, the modes L_j $(j = 1, 2, ...)$ behave similarly to the generalized Lamb waves, hence the letter L (when the plate is in vacuum, the modes are real and called Lamb modes). The region $\theta > \theta_C$ is occupied by the

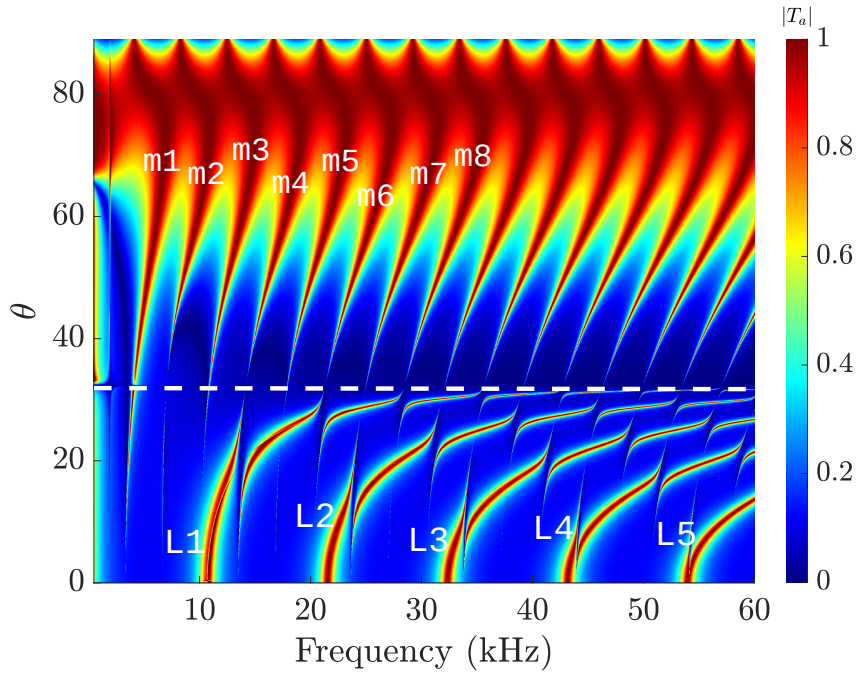

FIG. 3. (Colour on-line) Modulus of the transmission coefficient of a 2.865-cm-thick nonabsorbing EPS12 plate in air, in the frequency-angle of incidence plane (see data in Table I).

modes m_j ($j = 1, 2...$) which result from the micropolar nature of the material constituting the plate, hence the letter m (for generalized micropolar modes). Both generalized Lamb and micropolar modes indicate that the waves propagating in the plate are damped because some of the energy escapes from the plate to the surrounding fluid.

The form taken by the expressions of the reflection and transmission coefficients shows that it is difficult at this stage to precisely attribute a symmetric or antisymmetric character to the modes L_j and m_j (unlike the case of a plate obeying the equations of classical elasticity). As a corollary, in Fig. 2 as well as in Fig. 3, we notice the absence of two modes that should behave similarly to the well-known fundamental modes S_0 (symmetric) and A_0 (antisymmetric) of plates made of a classic elastic material (for example aluminum plate in

vacuum (Miklowitz, 1978) or in water (Überall, 1973)). The modes L_j ($j = 1, 2, ...$) have roughly the same form as the S_j and A_j of the aluminum plate. The modes m_j design in the plane (f, θ) a network of fairly close, quasi-vertical and equidistant modes originating at $\theta = 0°$ and partially overlapping when θ is approaching 90°. They represent a new kind of modes exclusively due to the micropolar effects.

It is important to note that a given mode m_j either does not interact with any of the L_j modes, or interacts with some particular L_j modes only. Thus, in Fig. 2 we can notice that the modes m_1 to m_7 do not interact with any mode L_j while in Fig. 3, it is the modes m_1, m_2, and m_3 that do not interact with any mode L_j. In Fig. 3 for example, the modes m_4, m_6 and the following of even index interact with the mode L_1, while the modes m_7 and m_9 and the following of odd index interact with the mode L_2 (with an even index) but not with L_1, the modes m_{10} and m_{12} of even index interact with the modes L_1, L_3, etc. To some extent, and with the appropriate adaptation, similar rules can be applied to the modes in Fig. 2 . Let us now specify the types of vibrations at the origin of the L_j modes.

For this purpose, let us briefly consider the case where the angle $\theta = 0$ (normal incidence), implying that $k_y = 0$. The dispersion equation for finding the eigenmodes of the micropolar plate in vacuum ($\Delta(k_y, f) = 0$) reduces to either $\tan(k_p h) = 0$ (antisymmetric modes) or $\cot(k_p h) = 0$ (symmetric modes) ($p = 1, 2$). The resolution of these equations provides the cutoff frequencies ${}^p f_{Acn}$ and ${}^p f_{Scn}$ of the modes ($n = 0, 1, 2, ...$). For the XPS plate, taking into account the thickness $2h = 3.5$cm and the velocity $c_1 = 1202$ m/s, we get (index S for symmetric, A for antisymmetric) ${}^1 f_{Sc0} = 17.17$kHz, ${}^1 f_{Sc1} = 51.51$kHz,... etc, ${}^1 f_{Ac0} = 0$, ${}^1 f_{Ac1} = 34.43$kHz, ${}^1 f_{Ac2} = 68.68$kHz...etc, while for the velocity $c_2 = 172.94$

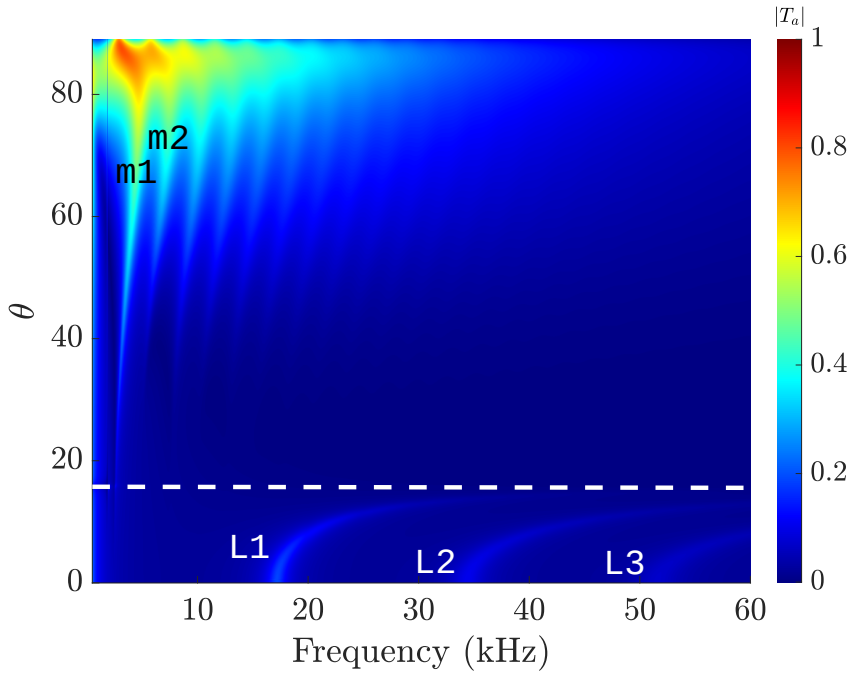

FIG. 4. (Colour on-line) Modulus of the transmission coefficient of a 3.5-cm-thick absorbing XPS plate in air, in the frequency-angle of incidence plane (see data in Table I).

m/s, ${}^2f_{Sc0} = 2.47$kHz, ${}^2f_{Sc1} = 7.4$kHz, ${}^2f_{Sc2} = 12.3$kHz... etc, ${}^2f_{Ac0} = 0$, ${}^2f_{Ac1} = 4.94$kHz, ${}^2f_{Ac2} = 9.88$kHz...etc. For the EPS12 plate, with the velocity $c_1 = 618$ m/s and the thickness $2h = 2.865$cm, it is found that ${}^1f_{Sc0} = 11$kHz, ${}^1f_{Sc1} = 33.13$kHz, ${}^1f_{Sc2} = 55.21$kHz... etc, ${}^1f_{Ac0} = 0$, ${}^1f_{Ac1} = 22$kHz, ${}^1f_{Ac2} = 44.17$kHz ...etc, while for $c_2 = 193$ m/s, ${}^2f_{Sc0} = 3.46$kHz, ${}^2f_{Sc1} = 10.38.13$kHz, ${}^2f_{Sc2} = 17.3$kHz... etc, ${}^2f_{Ac0} = 0$, ${}^2f_{Ac1} = 6.9$kHz, ${}^2f_{Ac2} = 13.84$kHz, etc.

By examining Figs. 2 and 3, we notice that these values are in agreement with the positions of the modes (when $\theta = 0$). In doing so, we have just shown directly that the L_p modes, with the odd p index are symmetric modes, while the modes with the even p index are antisymmetric modes. Recall that this recognition of the symmetric or antisymmetric

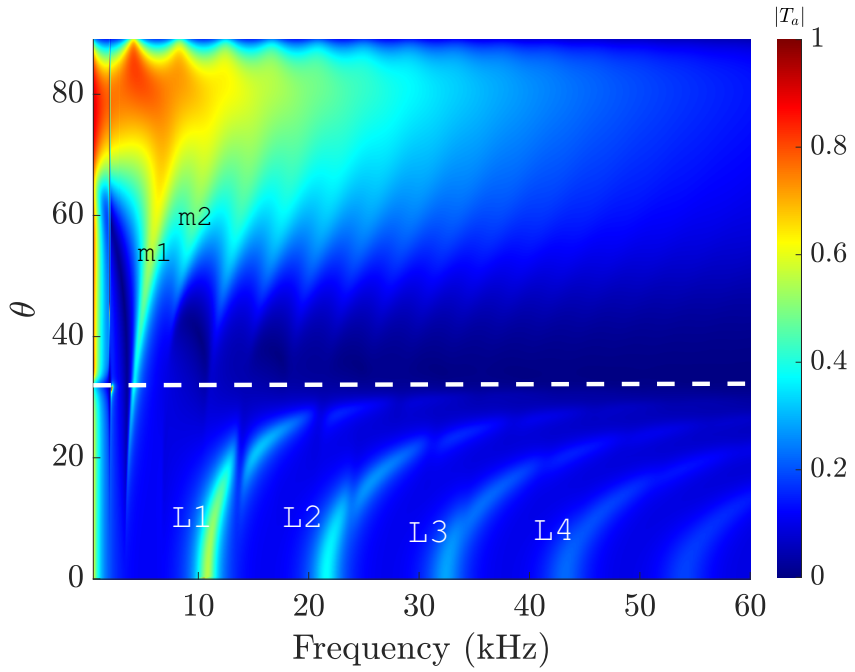

FIG. 5. (Colour on-line) Modulus of the transmission coefficient of a 2.865-cm-thick absorbing EPS12 plate in air, in the frequency-angle of incidence plane (see data in Table I).

character of a mode L_j (as well as a micropolar mode m_j) is direct using the matrix S method from Franklin *et al.* (2001) previously mentioned, see Fig. 2. It is a specificity of micropolar plates that modes L_j and m_j interact. In classical elasticity, the situation is quite different : the Lamb modes (which are divided into two families, one symmetric, another antisymmetric) and the curves of the same family never interact. Apart from the above two-dimensional reading, the two figures can be exploited either by considering at a fixed angle the variation of $|T_a|$ with the frequency, or by considering at a fixed frequency the variation of $|T_a|$ with the angle. Both points of view (frequency variable or angular variable) are important for the study of plate acoustic properties. In the experimental part of this paper, the behavior of the transmission coefficients in the frequency variable f (from 0 to

60 kHz) for the angles $\theta = 0°, 5°, 45°$ and $55°$ is shown. Based on the findings illustrated in Fig. 2 and 3, the incorporation of a hysteretic model representing the inherent damping characteristics of XPS and EPS panels involves introducing a scalar-valued loss factor into Young's modulus equation, defined as $E_d(\omega) = E_r(\omega) + iE_i(\omega) = E(\omega)(1 + i\chi(\omega))$ (where $E_r(\omega)$ denotes the storage modulus and $E_i(\omega)$ represents the loss modulus of the panel). By utilizing the specified values of χ, set to 0.02 for XPS and 0.06 for EP, as provided in the reference Ogam *et al.* (2021), the outcomes are depicted in Figs. 4 and 5, revealing the media's absorption properties.

VI. MATERIALS AND EXPERIMENTAL METHOD

The two samples (depicted in Fig. 6) used in our experiment, were both closed-cell polystyrene plates; however, there had been variation in their manufacturing process (see Ogam *et al.* (2021)). XPS was extruded, with a thickness of 3.5 cm, while EPS was expanded, with a thickness of 2.86 cm. These values are used above in the computations.

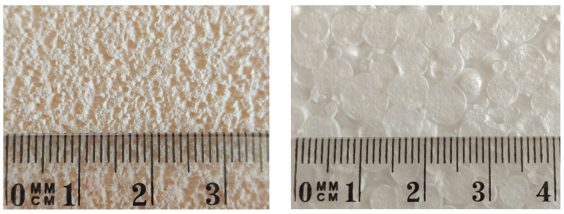

FIG. 6. Visualization of the plates (XPS on the left and EPS on the right).

Fig. 7 depicts all the equipment used for signal acquisitions. A pulse model 10 μs in width was generated from a generator (Agilent Technologies, 33220A, 20 MHz, Loveland, Colorado,

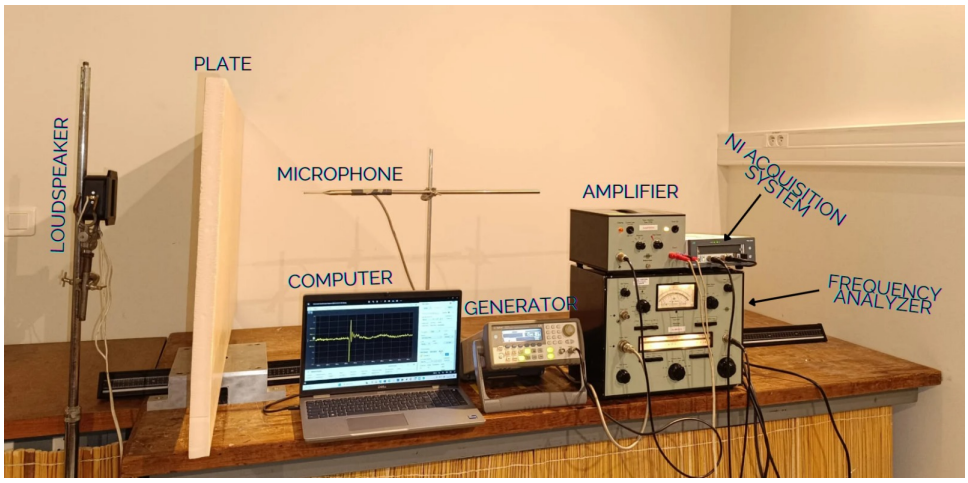

FIG. 7. Experimental setup.

USA) through a loudspeaker (Visaton, MHT 12). For the acquisition of the incident signal as well as of the transmitted signals at different incidence angles (from 0° to 60° with a step of 5° each time, we had to limit the incidence angle to 60° to avoid wave diffusion/diffraction, considering the geometric dimensions of the panels), a microphone (Brüel & Kjær, type 4138-C-006) was placed in series with a National Instruments acquisition system (type PXIe-1090). In order to obtain a better signal with these devices, we inserted a power amplifier (Brüel & Kjær, type 2706) between the generator and the loudspeaker, and a frequency analyzer (Brüel & Kjær, type 2121) between the microphone and the acquisition system. The transmission coefficients were obtained by calculating the estimated transfer function between the incident acoustic pressure (when there are no samples between the loudspeaker and the microphone) and those obtained with the samples for different angles.

The transmission coefficient was determined by analyzing the transfer function of a linear time-invariant (LTI) system, which represents the ratio between the incident pressure and the transmitted acoustic pressure. This coefficient, denoted as $|T_a|$, was derived by dividing

the cross-spectral power density S_{it} between the incident $p_i(t)$ and transmitted $p_t(t)$ acoustic pressures by the auto-spectral power density $S_{ii}(p_i(t))$

$$|\widetilde{T}_a(\omega)| = \frac{\widetilde{S}_{it}(\omega)}{\widetilde{S}_{ii}(\omega)} \tag{84}$$

Here, the tilde ($\tilde{}$) signifies that the function is an estimation. The quotient $|T_a|$ was computed using Matlab® tfestimate function with the acquired signals. To mitigate spectral leakage and ensure precise spectral measurements, the temporal signals were initially subjected to the windowing techniques developed by MathWorks (2002).

VII. RESULTS

A. Presentation of Results

The Figs. 8(a) and 8(b) depict the experimental incident and transmitted signals at normal incidence, in the time and frequency domain, respectively. It is noteworthy that the signal transmitted through the EPS plate is significantly more attenuated than the one transmitted through the XPS plate. Additionally, the signal transmitted through XPS precedes temporally the one transmitted through EPS, indicating a higher propagation velocity of the wave in XPS than in EPS. Furthermore, the more attenuated signal (EPS) exhibits greater temporal spreading, resulting in significant dispersion in the frequency domain. Specifically, the spectrum of EPS has lost a considerable portion of its high frequencies compared with the incident signal content, as illustrated in Fig. 8(b). Moreover, for XPS, several well-defined modes are present starting from 50 kHz, which are absent in the EPS spectrum. These modes overall justify the lesser attenuation observed in XPS in the time

domain. Fig. 9 presents the modulus of the transmission coefficient of the XPS plate in

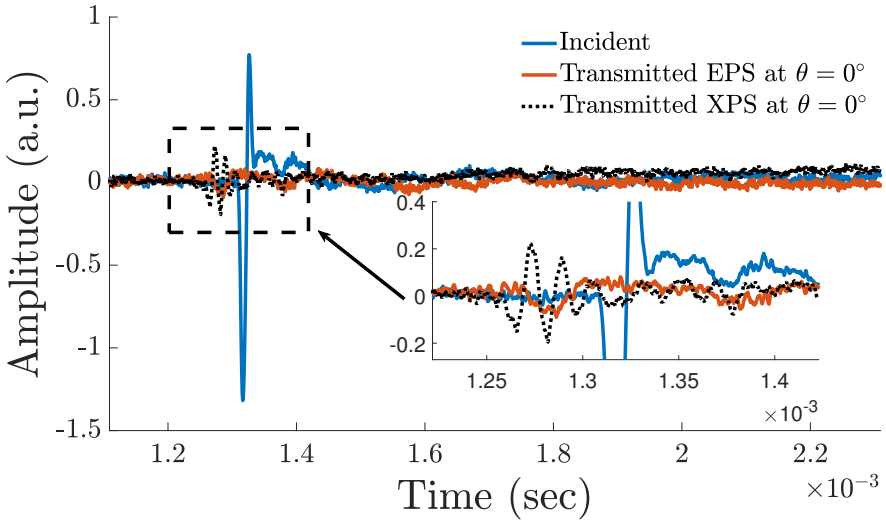

(a)

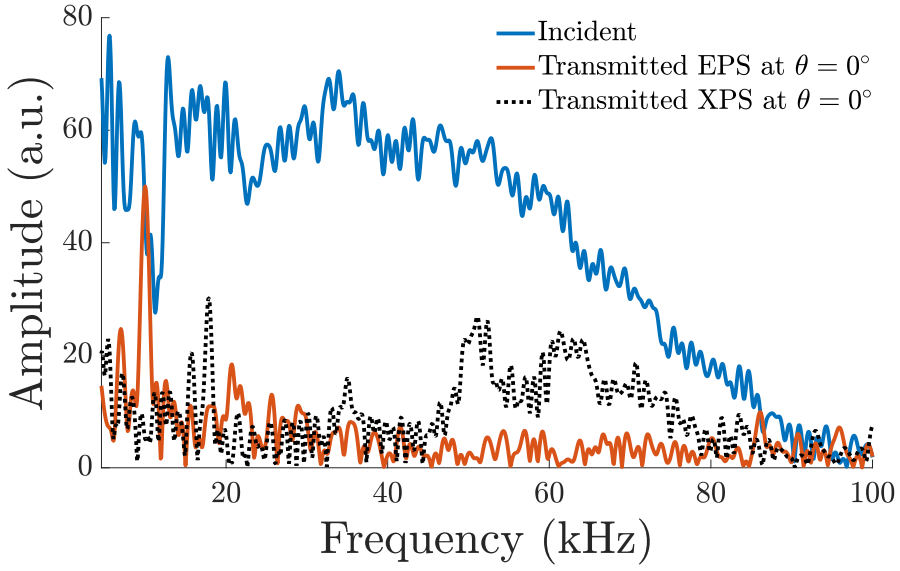

(b)

FIG. 8. Experimental signals in time (a) and frequency (b) domains from the XPS plate (3.5-cm-thick) and the EPS plate (2.86-cm-thick).

the frequency domain for incidence angles of 5° and 60°. At 5°, below the critical angle θ_C, only three Lamb modes appear up to 60 kHz, whereas at 60°, above θ_C, several additional

modes emerge within the same frequency range. The theoretical curves in Figs. 10(c) and 10(d) confirm this observation, showing significantly more modes above the critical angle compared to Figs. 10(a) and 10(b).

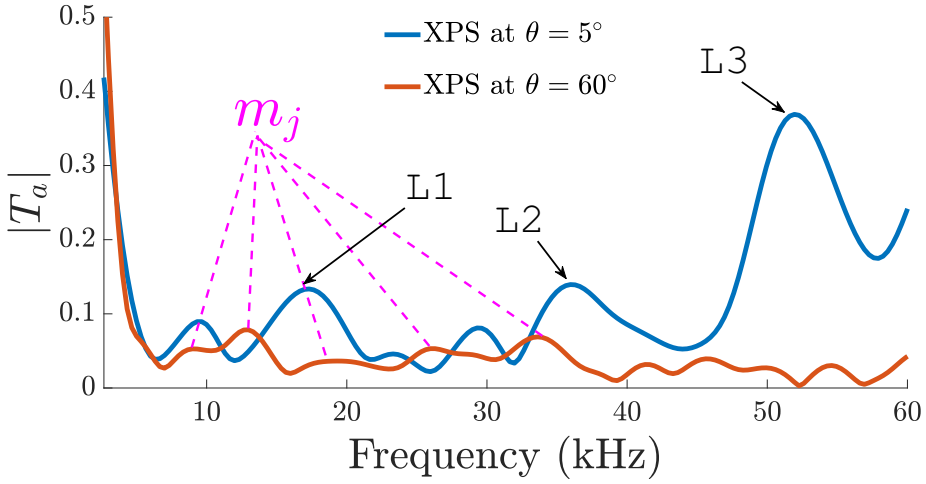

FIG. 9. Modulus of the experimental transmission coefficient $|T_a|$ of the XPS plate at 5° and 60°.

Figs. 10 and 11 compare, for the XPS plate and EPS plate, the modulus of the transmission coefficient in the frequency domain, based on theoretical and experimental data, for angles below (0° and 5°) and above (45° and 55°) the critical angle. The L_j modes are observed below θ_C, and the experimental data overall follow the theoretical trend as shown in Figs. 10(a), 10(b), 11(a), and 11(b). Above θ_C, as illustrated in Figs. 10(c), 10(d), 11(c), and 11(d), both the experimental results and the micropolar elasticity theory indicate propagation according to the m_j modes, in contrast to the classical theory where the wave is non-propagative beyond θ_C. Furthermore, as shown in Figs. 10 and 11, the discrepancies between theoretical and experimental resonance frequencies are overall small at low incidence angles, but increase as the incidence angle grows. It seems this is mainly due to the

anisotropic properties of such materials, as described by Inoue *et al.* (2007), which were not accounted for in the theoretical model. Table II presents the different frequencies for the first three Lamb modes at normal incidence.

TABLE II. Theoretical and experimental values of Lamb mode frequencies f_j at $\theta_C = 0°$.

Plate	$f_{1_{th}}$ (kHz)	$f_{1_{exp}}$ (kHz)	$f_{2_{th}}$ (kHz)	$f_{2_{exp}}$ (kHz)	$f_{3_{th}}$ (kHz)	$f_{3_{exp}}$ (kHz)
XPS	17.49	17	34.15	35	51.65	51
EPS	10.83	10	21.66	21	32.4	29

To better visualize and comprehend the evolution of vibration modes, we adopted a graphical representation where values vary based on frequency and incidence angle, presented in color on a grid in Figs. 12 and 13 for XPS and EPS. Despite significant attenuation in these media, we were able to identify at least the first three L_j modes. This representation offers the advantage of highlighting a transition zone between L_j and m_j modes around the critical angles, as predicted by theory in Section V, namely 15.93° for XPS and 32.25° for EPS. L_j modes are clearly observed from normal incidence at frequencies indicated in Table II. In Figs. 12 and 13 for EPS, we note that these frequencies generally increase with incident angle θ,while $|T_a|$ decreases, until reaching the transition zone where micropolar modes m_j emerge. The first m_1 modes are clearly identified in Fig. 12(b) for XPS and Fig. 13(a) for EPS. Notably, for XPS, a mode noted [m] is observed above θ_C starting from around 50 kHz, indicating one of the micropolar modes, although it is challenging to experimentally predict its order. For clarity, Fig. 12(b) (and respectively 13(b)) is a version of Fig. 12(a)

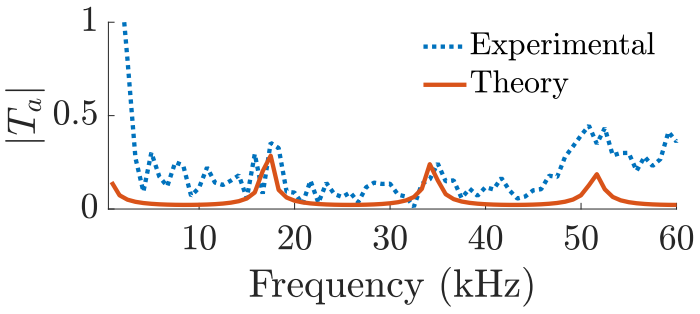

(a) $\theta = 0°$

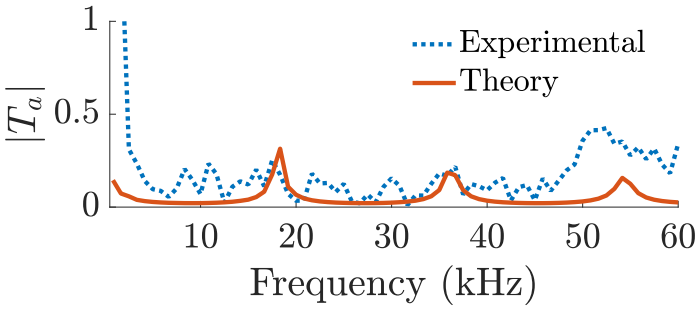

(b) $\theta = 5°$

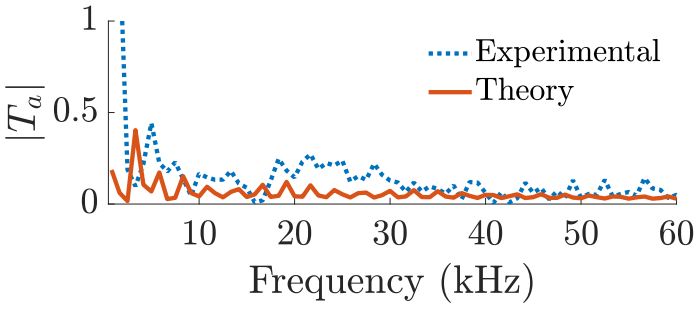

(c) $\theta = 45°$

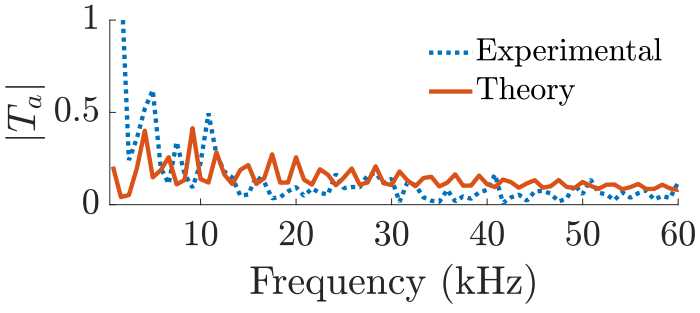

(d) $\theta = 55°$

FIG. 10. Modulus of the theoretical and experimental transmission coefficients for the 3.5-cm-thick XPS plate at various angles of incidence.

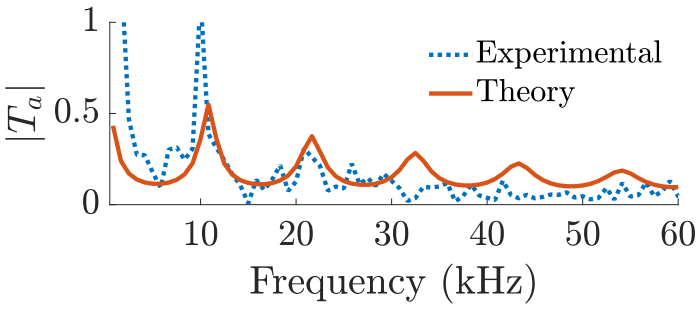

(a) $\theta = 0°$

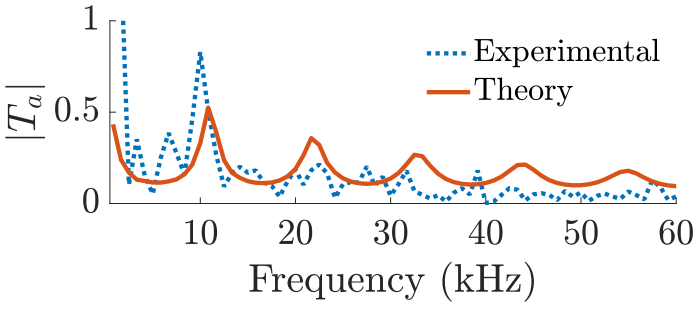

(b) $\theta = 5°$

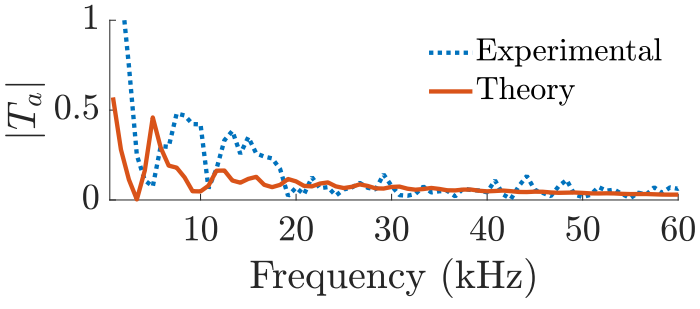

(c) $\theta = 45°$

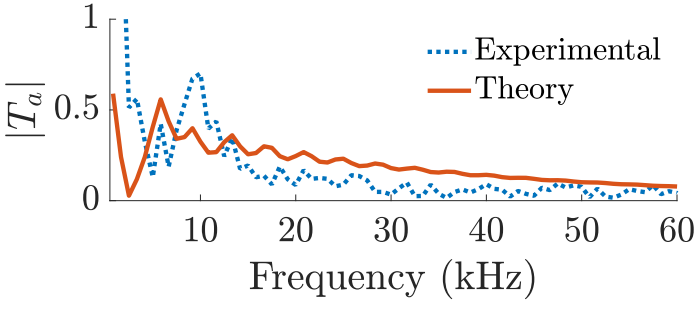

(d) $\theta = 55°$

FIG. 11. Modulus of the theoretical and experimental transmission coefficients for the 2.86-cm-thick EPS plate at various angles of incidence.

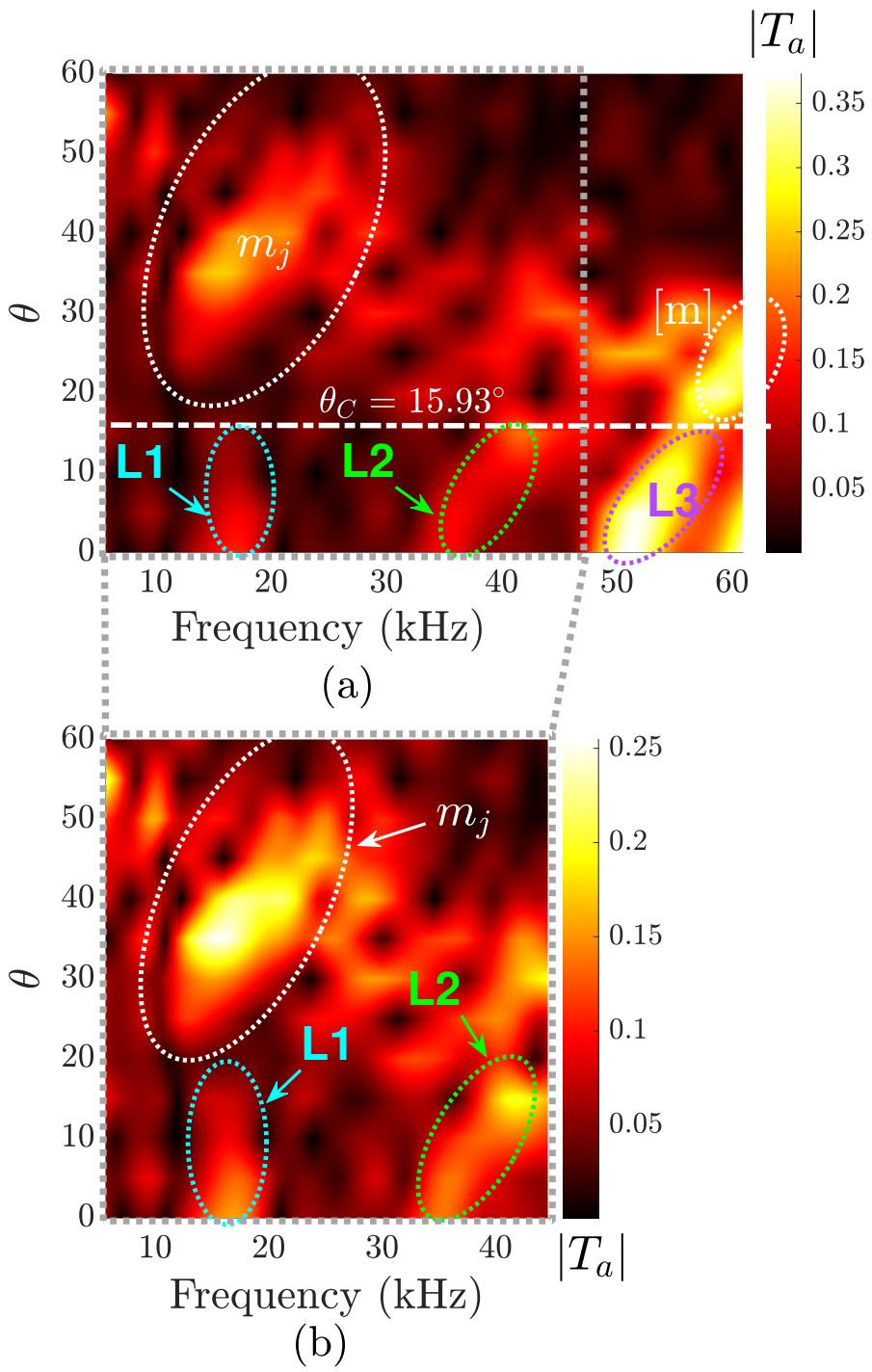

FIG. 12. Experimental measurement of the evolution of the vibration modes of the 3.5-cm-thick XPS plate. (b) is an highlight on the 1st and 2nd L_j modes.

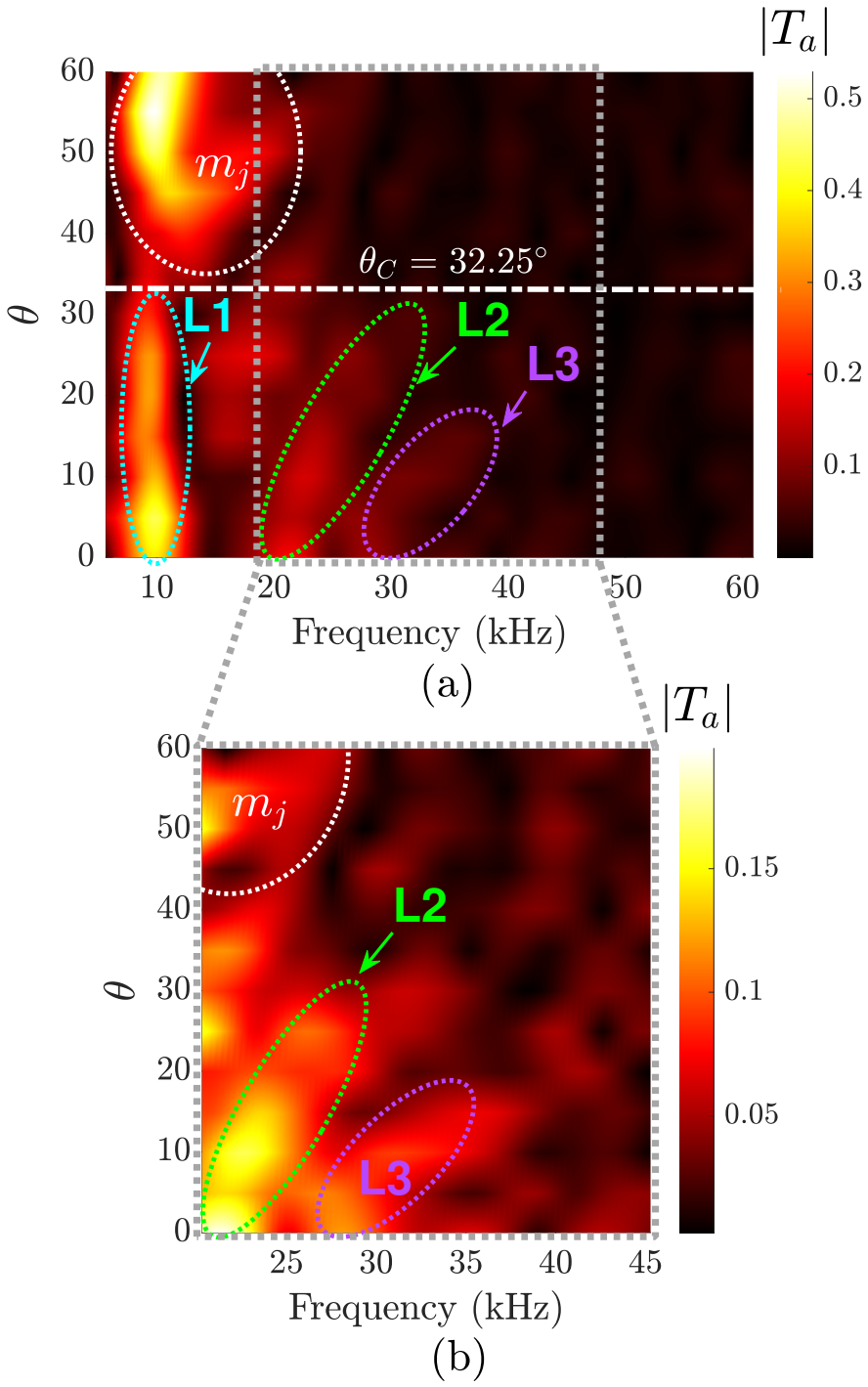

FIG. 13. Experimental measurement of the evolution of the vibration modes of the 2.86-cm-thick EPS plate. (b) is an highlight on the 2nd and 3rd L_j modes.

(and respectively 13(a)) limited to a frequency band, allowing for a better visualization of the evolution of L_1 and L_2 modes of the XPS panel (and respectively L_2 and L_3 of the EPS panel) at a high visual intensity scale.

B. Discussions and application

In this work, through experiments, we first observed the classical modes L_1, L_2, and L_3 below the critical angle θ_C, at frequencies overall close to the theoretical results. We limited the experiments to 60° to ensure reliable results by avoiding edge diffraction from the sample due to its finite size. Then, we observed a new phenomenon : the propagation modes beyond θ_C, contrary to what is predicted by the classical theory. However, we have demonstrated their theoretical prediction within the framework of micropolar theory. We estimate that it is not possible at this stage to precisely identify the different new modes m_1, m_2, m_3, etc., at well-determined frequencies in comparison with theory, for the following reasons : (i) unlike in theory, experimentally, we are limited in frequency, both at high and low ends. Indeed, below 4 kHz, we do not have sufficient energy distribution to obtain information about the medium. Thus, all experimental results are restricted to a range of 4 to 60 kHz, (ii) from a theoretical perspective, the frequency gaps between two successive modes m_j are very small, and we believe that in the experimental observations shown in Figs. 12 and 13, their boundaries overlap, giving the impression of observing a single, more extended mode in frequency, (iii) some physical characteristics of real materials were not accounted for in the theoretical model, such as anisotropy and heterogeneity. For instance, Young's modulus

is not expected to be uniform in all directions, (iv) the absorption model needs to be studied in parallel with the experiments.

We believe that precise localization of these new modes in the frequency domain will require a more in-depth characterization study of the medium. This includes mastering the influence of each parameter on the new micropolar modes, understanding their sensitivity to variations in the characteristic parameters of the micropolar medium, and examining the complex interactions between these factors. Additionally, assessing their potential impact on the alignment between theory and experiment is a key future prospect.

These findings are of significant importance as they enhance our understanding of these materials, often used in buildings for sound absorption and thermal insulation purposes. Indeed, during building design, the arrangement of facades relative to the sound source could now consider not only the position corresponding to the critical angle, but also the potential appearance of new, more intense propagation modes beyond this angle for elastic materials exhibiting micropolar behavior. These modes could otherwise lead to undesirable resonances. This research opens opportunities to develop more realistic prediction tools, as these modes are not currently accounted for in existing tools. This would therefore enable the development of new designs and optimized solutions.

VIII. CONCLUSIONS

Using a combined theoretical and experimental approach, this study investigates the acoustic transmission properties of plates assumed to adhere to the theory of micropolar media. The theoretical transmission coefficient is formulated to highlight terms reminiscent

of those encountered in the examination of generalized Lamb modes of classical linear elastic plates, as well as terms indicating a novel type of vibration modes referred to as micropolar modes. Overlaying diverse transmission coefficients for different angles of incidence (ranging from 0 to 60°) provides insights into the behavior of the micropolar modes, aiding in understanding mode evolution in the frequency domain and estimating critical angles. As micropolar plates, two types of low-density closed-cell foam panels made from polystyrene are utilized : one expanded (referred to as EPS) and the other extruded (referred to as XPS). The frequency domain of study spans from 4 to 60 kHz, employing a tweeter loudspeaker and a microphone integrated with a National Instruments acquisition system. This facilitates the identification, for each plate, of the modulus of the transmission coefficient, starting from normal incidence : (i) at least the first three Lamb modes (located below the critical angle relative to the fastest phase velocity), and (ii) the micropolar modes (extending on each side of the critical angle, although the experimentally observable branches lie above the critical angle). Due to significant attenuation in the medium, the measurements show that the intensity of the modes decreases as the frequency increases, except in the case of the XPS plate, which stands out from the EPS in the observation of dynamic phenomena. Indeed, for XPS, the higher modes, such as the classical L_3 and the micropolar mode $[m]$ beyond θ_C, exhibit greater intensities than the previous modes. Consequently, the agreement between the experimental and theoretical results was not completely aligned. This can be explained by the heterogeneity and anisotropy of the materials used (see Ashby and Gibson (1997); Inoue *et al.* (2007)), which were not accounted for in the theoretical model, as well as the absorption model employed, which does not fully align the observations, particularly for

the XPS plate. These factors represent a research avenue for improving the modeling. The novelty of this paper lies in two aspects : it provides theoretical predictions of micropolar modes, and their experimental observation above a critical angle of incidence. Overall, this research offers insights into the properties of these materials commonly used in industry and construction, particularly regarding their role in thermal and acoustic insulation.

ACKNOWLEDGMENTS

The first author expresses gratitude to the French Embassy in the Democratic Republic of Congo for their financial support through the "Bourse du Gouvernement Français (BGF)", which enabled this research, and to the Polytechnic Faculty of the University of Kinshasa for their assistance in training.

AUTHOR DECLARATIONS

The authors declare that they have no conflicts of interest to disclose in the context of this research. They also affirm that their work adheres to ethical approval, indicating that their research does not involve experiments on animal subjects and/or human participants.

DATA AVAILABILITY

Data is available upon request from the authors. The information supporting the findings of this study is accessible from the corresponding author upon reasonable request.

Ashby, M. F., and Gibson, L. J. (**1997**). "Cellular solids: structure and properties," Press Syndicate of the University of Cambridge, Cambridge, UK 175–231.

Cosserat, E., and Cosserat, F. (**1909**). *Théorie des corps déformables* (A. Hermann et fils).

Eringen, A. C. (**1966**). "Linear theory of micropolar elasticity," Journal of Mathematics and Mechanics 909–923.

Eringen, A. C. (**1999**). *Theory of micropolar elasticity* (Springer).

Eringen, A. C. (**2012**). *Microcontinuum field theories: I. Foundations and solids* (Springer Science & Business Media).

Fiorito, R., Madigosky, W., and Überall, H. (**1979**). "Resonance theory of acoustic waves interacting with an elastic plate," The Journal of the Acoustical Society of America **66**(6), 1857–1866.

Franklin, H., Danila, E., and Conoir, J.-M. (**2001**). "S-matrix theory applied to acoustic scattering by asymmetrically fluid-loaded elastic isotropic plates," The Journal of the Acoustical Society of America **110**(1), 243–253.

Hassanpour, S., and Heppler, G. R. (**2017**). "Micropolar elasticity theory: a survey of linear isotropic equations, representative notations, and experimental investigations," Mathematics and Mechanics of Solids **22**(2), 224–242.

Inoue, R., Kanaya, T., Nishida, K., Tsukushi, I., Taylor, J., Levett, S., and Gabrys, B. (**2007**). "Dynamic anisotropy and heterogeneity of polystyrene thin films as studied by inelastic neutron scattering," The European Physical Journal E **24**, 55–60.

Kafadar, C., and Eringen, A. C. (**1971**). "Micropolar media—i the classical theory," International Journal of Engineering Science **9**(3), 271–305.

Koiter, W. (**1969**). "Couple-stresses in the theory of elasticity, i & ii," .

Kumar, R., Tomar, S. K. *et al.* (**2001**). "Reflection and transmission of elastic waves at viscous liquid/micropolar elastic solid interface," International Journal of Mathematics and Mathematical Sciences **26**, 685–694.

MathWorks, I. (**2002**). *Signal Processing Toolbox for Use with MATLAB: User's Guide* (The MathWorks).

Maugin, G. A., and Metrikine, A. V. (**2010**). "Mechanics of generalized continua," .

Miklowitz, J. (**1978**). "Elastic waves and waveguides," .

Mindlin, R. (**1965**). "Stress functions for a cosserat continuum," International Journal of Solids and Structures **1**(3), 265–271.

Mindlin, R. D., Tiersten, H. *et al.* (**1962**). "Effects of couple-stresses in linear elasticity," Archive for Rational Mechanics and analysis **11**(1), 415–448.

Ogam, E., Fellah, Z. E. A., Fellah, M., and Depollier, C. (**2021**). "Theoretical and experimental study of micropolar elastic materials using acoustic waves in air," Journal of Sound and Vibration **510**, 116298.

Parfitt, V. R., and Eringen, A. (**1969**). "Reflection of plane waves from the flat boundary of a micropolar elastic half-space," The Journal of the Acoustical Society of America **45**(5), 1258–1272.

Singh, D., and Tomar, S. (**2008**). "Longitudinal waves at a micropolar fluid/solid interface," International Journal of Solids and Structures **45**(1), 225–244.

Toupin, R. (**1962**). "Elastic materials with couple-stresses," Archive for rational mechanics and analysis **11**(1), 385–414.

Überall, H. (**1973**). "Surface waves in acoustics," in *Physical acoustics*, **10** (Elsevier), pp. 1–60.

Viktorov, I. A. (**1967**). "Rayleigh and lamb waves," Rayleigh and Lamb Waves 33.